Journal of Biomechanics 166 (2024) 112058

Contents lists available at ScienceDirect

Journal of Biomechanics

journal homepage: www.elsevier.com/locate/jbiomech

Post-angioplasty remodeling of coronary arteries investigated via a chemo-mechano-biological *in silico* model

Meike Gierig [a], Pierfrancesco Gaziano [b], Peter Wriggers [a], Michele Marino [b,*]

[a] Institute of Continuum Mechanics, Leibniz University of Hannover, An der Universität 1, 30823 Garbsen, Germany
[b] Department of Civil Engineering and Computer Science Engineering, University of Rome Tor Vergata, Via del Politecnico 1, 00133 Rome, Italy

ARTICLE INFO

Keywords:
Chemo-mechano-biological model
Tissue inflammatory response
Balloon angioplasty
Vessel remodeling
In silico medicine

ABSTRACT

This work presents the application of a chemo-mechano-biological constitutive model of soft tissues for describing tissue inflammatory response to damage in collagen constituents. The material model is implemented into a nonlinear finite element formulation to follow up a coronary standard balloon angioplasty for one year. Numerical results, compared with available *in vivo* clinical data, show that the model reproduces the temporal dynamics of vessel remodeling associated with subintimal damage. Such dynamics are bimodular, being characterized by an early tissue resorption and lumen enlargement, followed by late tissue growth and vessel constriction. Applicability of the modeling framework in retrospective studies is demonstrated, and future extension towards prospective applications is discussed.

1. Introduction

The clinical context of this work is restenosis, a prominent side effect of balloon angioplasty. Restenosis is the artery renarrowing within the first year after the treatment, and it is also referred to as negative or constrictive vessel remodeling (Pasterkamp et al., 2000). It might lead to the need of re-intervention with a reported incidence of 25% to 50% if not accompanied by stent insertion (Jukema et al., 2012).

Clinical studies extensively document a bimodal temporal dynamics of changes in lumen diameter after balloon angioplasties, with an early lumen enlargement followed by vessel restriction (Nobuyoshi et al., 1988; Kimura et al., 1997; Kleber et al., 2015; Ueno et al., 2023). Evidence of this behavior is found, e.g., in the clinical study by Nobuyoshi et al. (1988), discussed in Fig. 1. Early lumen enlargement, also known as positive (or adaptive, expansive) vessel remodeling, aligns with the compensatory arterial dilatation observed in the early stages of atherosclerosis (Glagov et al., 1987). Importantly, the absence of positive vessel remodeling is identified as a major determinant of restenosis in animal studies (Kakuta et al., 1994; Mintz et al., 1996).

After angioplasty, complex alterations in the turnover of tissue constituents occur, also characterized by bimodal temporal dynamics, leading to changes in composition and structure of arterial tissues (Pasterkamp et al., 2000). At the onset of tissue injury, the extracellular matrix (ECM) takes the lead in orchestrating the repair of the affected site by modulating cellular behavior. Enhanced breakdown of ECM just after angioplasty is followed by increased matrix production in the long term. Molecular mediators, such as growth factors (GFs) and matrix metalloproteinases (MMPs), are activated and synthesized, creating a dynamic cascade of events that further stimulate cellular responses and ECM modifications (Davis et al., 2003; Berridge, 2012; Mouw et al., 2014). Some major actors of this process, addressed in the present work, are schematically depicted in Fig. 1. Quantitative insights on the relationship between early tissue resorption and early lumen arrangement, as well as between late tissue growth and restenosis remain limited. This knowledge gap hinders the development of therapeutic interventions targeting these mechanisms (Kleber et al., 2018).

In fact, restenosis involves two distinct, possibly highly coupled, mechanisms (Jukema et al., 2012; Koskinas et al., 2012). One emphasizes alterations in blood-flow-related shear stresses and thrombogenic risk, while the other focuses on vessel wall damage triggering inflammation and abnormal growth. In the latter, endothelial denudation and subintimal damage are key sources of damage. While endothelial denudation is well-studied, the exploration of subintimal damage is less extensive. Clear evidence indicates collagen damage within the media due to tissue overstretch during vessel inflation (Converse et al., 2018; Marino et al., 2019). Subsequently, inflammatory mechanisms are activated to replace the damaged collagen, coupling with remodeling stimuli driven by homeostatic principles that maintain the *in vivo* pre-stressed state.

The dynamics of tissue remodeling post-angioplasty is mainly associated with collagen turnover (Pasterkamp et al., 2000). Vascular

* Corresponding author.
E-mail address: m.marino@ing.uniroma2.it (M. Marino).

https://doi.org/10.1016/j.jbiomech.2024.112058
Accepted 21 March 2024
Available online 24 March 2024
0021-9290/© 2024 The Author(s). Published by Elsevier Ltd. This is an open access article under the CC BY-NC-ND license (http://creativecommons.org/licenses/by-nc-nd/4.0/).

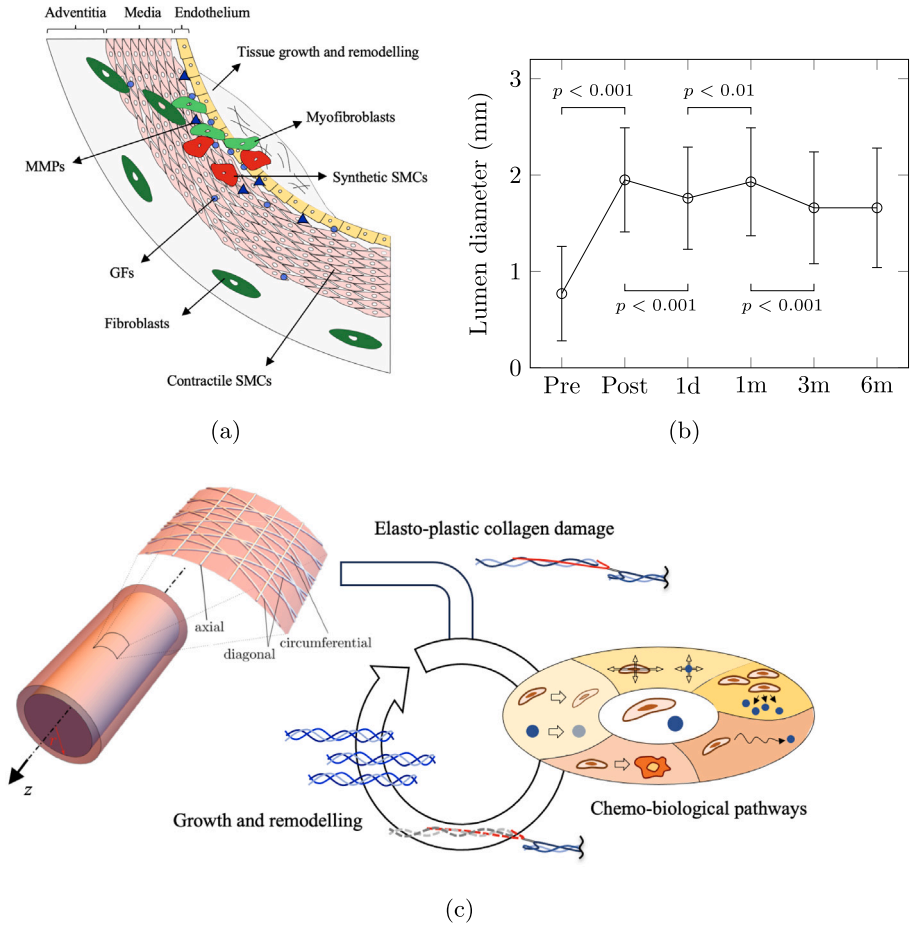

Fig. 1. Post-angioplasty chemo-mechano-biology of tissue turnover. (a) Schematic description of the main actors involved in the intricate process of tissue repair following injury. Acronyms: matrix metalloproteinases (MMPs), growth factors (GFs), smooth muscle cells (SMCs). (b) Clinical data by Nobuyoshi et al. (1988) from follow-up measurements of the narrowest inner radius in stenosed segments of human coronary arteries after angioplasty, measured by quantitative coronary angiography. Reported evidence refer to $n = 185$ patients with follow-up measurements taken before intervention (Pre), after the procedure (Post), at day 1 and at months 1, 3, and 6. Data confirm that angioplasty significantly widens the internal lumen (Pre-to-Post). On the first day, some of the gained inner diameter is lost due to viscoelastic recover (Post-to-1d). An increase in inner diameter is observed during the first month (1d-to-1m). Stenosis diameter decreased markedly from month 1 to 3 (1m-to-3m). All these differences are statistically significant. On the other hand, stenosis diameter was similar from month 3 to 6 (3m-to-6m). In the original paper, it was also shown that no significant change in stenosis diameter was observed from 6 months to 1 year. (c) General rationale of the proposed chemo-mechano-biological model of tissue inflammatory response to balloon angioplasty in arterial segments.

mechanical properties after balloon angioplasty are minimally affected by intimal injury but substantially influenced by collagen damage and turnover. Consequently, the intricate interplay between mechanics, inflammation's chemo-biology, and tissue remodeling is most pronounced when considering collagen damage and turnover, presenting considerable challenges in computational modeling.

The present study explores the tissue inflammatory response associated with restenosis, particularly focusing on subintimal damage. It is essential to note that our goal is not to offer a comprehensive description of restenosis as we acknowledge that the combined influence of shear stresses, thrombogenic phenomena, endothelial denudation, and subintimal damage should likely be considered for a more thorough understanding.

1.1. State-of-the-art on computational models

Computational models are promising tools to better understand the restenosis behavior and to identify key players for a predictive assessment (Ninno et al., 2023). Modeling of restenosis involves the description and coupling of nonlinear tissue elasticity (Humphrey, 2013; Marino, 2019), damage (Kachanov, 1986; Balzani et al., 2006; Gasser and Holzapfel, 2002; Marino et al., 2019), growth and remodeling (Humphrey and Rajagopal, 2002; Cyron et al., 2016; Braeu et al., 2019), and biological and cell mechanisms (Buganza Tepole and Kuhl, 2016; Escuer et al., 2019; Loerakker and Ristori, 2019).

Several computational models addressing the restenosis process can be found in the literature. Some present a refined mechanical description but neglect molecular and cell biological pathways (Fereidoonnezhad et al., 2017; He et al., 2019b, 2020). We address here only those coupling chemo-mechano-biological mechanisms.

For instance, Escuer et al. (2019) presented a two-dimensional continuum-based model that accounts for the interaction of GFs and MMPs with various cellular and extracellular components, together with the presence of a stent. McQueen et al. (2022) further analyzed drug effects using this model. However, this model does not consider chemotaxis, a critical factor in cell redistribution within tissues especially at the damage site. Additionally, it solely attributes growth to endothelial denudation and consider the tissue as isotropic. Furthermore, it neglects the continuous exposure of tissues to homeostasis-driven remodeling stimuli.

Corti et al. (2021, 2022, 2023) couple continuum-based simulations of structural and fluid mechanical aspects with agent-based models (ABM) for the system biology driving restenosis. These models have demonstrated success in patient-specific case studies, particularly in tracking one-year in-stent restenosis in superficial femoral

arteries (Corti et al., 2023). However, these models focus only on endothelial-level tissue damage. Furthermore, molecular pathways are neglected, and only phenomenologically described by means of *ad hoc* probabilistic ABM laws. Additionally, ABMs inherently struggle to capture the influence of internal stresses in the process, limiting the application of growth and remodeling frameworks that provide a theoretically consistent description of the phenomenon (Humphrey and Rajagopal, 2002; Cyron et al., 2016; Braeu et al., 2019). Furthermore, the homeostasis-driven remodeling stimulus is neglected. It is essential to acknowledge that ABMs offer distinct advantages, which are clearly not questioned here.

Manjunatha et al. (2022, 2023) have recently presented a fully-coupled chemo-mechano-biological continuum description of the restenosis process, even including the effects of drugs. However, also in this case only endothelial damage is addressed and the homeostasis-driven tissue remodeling is neglected. Moreover, damage is assigned *a priori* as a given initial condition since the balloon angioplastic procedure is not simulated.

While the previous methods produce intriguing findings, the reported results do not capture the bimodal nature of the dynamics of lumen area and tissue remodeling. This distinctive behavior is instead reproduced by the computational model proposed by Maes et al. (2021). They introduce a homogenized constrained mixture growth and remodeling framework, which incorporates homeostasis-driven remodeling coupled with a chemo-biological model of restenosis by Boyle et al. (2011). However, like previously-discussed approaches, this model exclusively considers endothelial damage. Moreover, it treats each agent in the chemo-biological model as a local entity, thereby ignoring cell migration and molecular diffusion. The same limitation applies to the study by Gierig et al. (2021).

1.2. Hypothesis-driven goal

We hypothesize that subintimal damage and the consequent tissue remodeling are pivotal in driving the dynamics of the restenosis process, contributing significantly to its bimodal nature. To validate this hypothesis, we employ a chemo-mechano-biological *in silico* model previously introduced by Gierig et al. (2023) to simulate tissue inflammation and remodeling subsequent to balloon angioplasty in coronary arteries. Notably, we address aspects that have been overlooked in the current state of the art.

The model encompasses finite deformations, plastic deformation of collagen fibers as a source of subintimal damage, tissue remodeling to restore a preferred stretch state, and growth inspired by the homogenized constrained mixture theory. Everything is coupled through a chemo-biological model. The latter accounts for the roles of MMPs, GFs, and cellular species in proliferation, chemotaxis, and phenotype switch. Our numerical results align with clinical data, allowing to reproduce the complex dynamics of early tissue resorption and late tissue growth, underscoring the model's potential in reproducing both compensatory arterial dilatation and restenosis mechanisms.

2. Materials and methods

The main features of the chemo-mechano-biological model previously introduced by Gierig et al. (2023) are schematically depicted in Fig. 1(c) and described in Sections 2.1 to 2.5. Additional information can be found in the original paper, to which interested readers are referred. In Section 2.6, we present the specialization of the proposed computational framework for modeling restenosis after balloon angioplasty. This case study, along with its associated numerical results, is original and distinct from previously published material.

The model is based on a nonlinear continuum mechanics framework. A material point $\mathbf{X}$ in the reference configuration is mapped by $\mathbf{x} = \varphi(\mathbf{X}, t)$ to the corresponding point in the current configuration at time t via the transformation φ. The deformation gradient is denoted by $\mathbf{F} = \nabla_{\mathbf{X}}\varphi = \partial\varphi/\partial\mathbf{X}$, with $J = \det(\mathbf{F})$ being its Jacobian, $\mathbf{C} = \mathbf{F}^T\mathbf{F}$ is the corresponding right Cauchy–Green deformation tensor. Let ρ_0 be the total tissue mass per unit volume in the reference configuration, referred to as reference density, and $\rho = \rho_0/J$ the corresponding measure in the current configuration, known as spatial tissue density. Growth induces changes in the total mass of the tissue, leading to a spatio–temporal dependency $\rho_0 = \rho_0(\mathbf{X}, t)$. Finally, $\nabla_{\mathbf{X}}\cdot$ denotes the divergence operator in the reference configuration, $\dot{f}$ the material time derivative of function f, and $\langle\cdot\rangle$ the Macaulay brackets.

2.1. Elasto-plastic behavior and homeostasis-driven remodeling

The extracellular matrix is considered to be a mixture of non-collageneous constituents (superscript m) with reference density ρ_0^{m}, and 4 families of collagen fibers (superscript c). Collagen fibers are treated as unidimensional reinforcements with total reference mass densities ρ_0^{c}. The stretch along the main direction of the j–th fiber family is denoted by λ_j^{c}. With respect to a cylindrical coordinate reference system where the z direction is aligned with vessel centerline (see Fig. 1(c)), the 4 families of fibers are oriented along the circumferential direction (reference density $\rho_{0\phi}^{\mathrm{c}}$), the axial direction (reference density ρ_{0z}^{c}), and along the diagonal directions at $\pm 45°$ with respect to the circumferential direction in the (ϕ, z)-plane (reference densities $\rho_{0d_1}^{\mathrm{c}} = \rho_{0d_2}^{\mathrm{c}} = (\rho_0^{\mathrm{c}} - \rho_{0z}^{\mathrm{c}} - \rho_{0\phi}^{\mathrm{c}})/2$).

Constituents experience the same total deformation gradient $\mathbf{F}$, but individual elastic and inelastic deformations, namely:

$$\mathbf{F} = \mathbf{F}_{\mathrm{e}}^{\mathrm{m}} = \mathbf{F}_{\mathrm{e}_1}^{\mathrm{c}}\,\mathbf{F}_{\mathrm{r}_1}^{\mathrm{c}}\,\mathbf{F}_{\mathrm{p}_1}^{\mathrm{c}} = \cdots = \mathbf{F}_{\mathrm{e}_4}^{\mathrm{c}}\,\mathbf{F}_{\mathrm{r}_4}^{\mathrm{c}}\,\mathbf{F}_{\mathrm{p}_4}^{\mathrm{c}}\,. \tag{1}$$

Here, the non-collagenous matrix is assumed to deform purely elastically ($\mathbf{F}_{\mathrm{e}}^{\mathrm{m}}$) since it is mainly comprised of elastin. The j–th collagen fiber family experiences both elastic ($\mathbf{F}_{\mathrm{e}_j}^{\mathrm{c}}$) and inelastic mechanisms. In turn, these latter comprise:

1. damage of collagen fibers, associated with fiber-specific plastic deformations $\mathbf{F}_{\mathrm{p}_j}^{\mathrm{c}}$. These are isochoric and described through the (permanent) plastic stretch $\lambda_{\mathrm{p}_j}^{\mathrm{c}}$ in the fiber direction. Fiber plastic stretch is governed by the damage variable d_j, that increases from 0 (no damage, purely elastic response) to 1 (completely damaged, perfectly plastic response). In turn, damage evolves when the maximum fiber stretch $\lambda_{\max,j}^{\mathrm{c}}$, reached during the loading history, exceeds threshold $\bar{\lambda}_{\mathrm{p}}$ and is linearly proportional to the difference $(\lambda_{\max,j}^{\mathrm{c}} - \bar{\lambda}_{\mathrm{p}})$ through constant m_{p} (Marino et al., 2019);
2. homeostasis-driven remodeling of collagen fibers, leading to fiber-specific inelastic deformations $\mathbf{F}_{\mathrm{r}_j}^{\mathrm{c}}$. Such deformations are isochoric and can be described through the permanent stretch $\lambda_{\mathrm{r}_j}^{\mathrm{c}}$ in the direction of the fiber family. The latter evolves through an evolution equation defined to maintain a preferred elastic prestretch $\lambda_{\mathrm{pre}}^{\mathrm{c}}$ with time constant k_r (Grytsan et al., 2017). It is noteworthy that the collagen mass change associated with this mechanism is null, that is $\dot{\rho}_{0_j}^{\mathrm{c}} = 0$.

Neglecting body forces, the balance of linear momentum reads:

$$\nabla_{\mathbf{X}} \cdot (\mathbf{F}\mathbf{S}) = \mathbf{0}\,, \tag{2}$$

where the second Piola–Kirchhoff stress tensor $\mathbf{S}$ is given by:

$$\mathbf{S} = 2\rho_0^{\mathrm{m}}\frac{\partial W^{\mathrm{m}}}{\partial \mathbf{C}} + 2\sum_{j=1}^{4}\rho_{0_j}^{\mathrm{c}}\frac{\partial W_j^{\mathrm{c}}}{\partial \mathbf{C}}\,. \tag{3}$$

Here, W^{m} represents the strain–energy density (per unit mass) of the non-collagenous matrix, modeled through an isotropic and isochoric Neo-Hookean expression (with stiffness constant μ). Moreover, W_j^{c} represents the strain–energy density (per unit mass) of collagen fibers, modeled through anisotropic Holzapfel-like exponential terms (with stiffness modulus k_1 and stiffening parameter k_2). Clearly, strain-

energies depend on the elastic deformation of constituents, hence resulting $W^{\mathrm{m}} = W^{\mathrm{m}}(\mathbf{C}^{\mathrm{m}}_{\mathrm{e}})$ with $\mathbf{C}^{\mathrm{m}}_{\mathrm{e}} = (\mathbf{F}^{\mathrm{m}}_{\mathrm{e}})^T\mathbf{F}^{\mathrm{m}}_{\mathrm{e}}$ and $W^{\mathrm{c}}_j = W^{\mathrm{c}}_j(\mathbf{C}^{\mathrm{c}}_{\mathrm{e}_j})$ with $\mathbf{C}^{\mathrm{c}}_{\mathrm{e}_j} = (\mathbf{F}^{\mathrm{c}}_{\mathrm{e}_j})^T\mathbf{F}^{\mathrm{c}}_{\mathrm{e}_j}$.

2.2. Tissue damage and inflammatory mechanisms

When considering an injurious event like balloon angioplasty, damage and inflammatory mechanisms occur at two very different time scales. Damage occurs within the time-frame $t \in [0, t^*]$, lasting seconds or few minutes, while the inflammatory response takes hours, days or months. At the end of the damaging phase, the amount of damaged and non-damaged collagen for each fiber family can be quantified by their reference densities, respectively denoted by $\rho^{\mathrm{cd}*}_{0_j}$ and $\rho^{\mathrm{ci}*}_{0_j}$. Such values are obtained from the value of the damage variable d_j at time $t = t^*$ as:

$$\rho^{\mathrm{cd}*}_{0_j}(\mathbf{X}) = d_j(\mathbf{X}, t^*)\bar{\rho}^{\mathrm{c}}_{0_j}\,, \tag{4a}$$

$$\rho^{\mathrm{ci}*}_{0_j}(\mathbf{X}) = \left[1 - d_j(\mathbf{X}, t^*)\right]\bar{\rho}^{\mathrm{c}}_{0_j}\,. \tag{4b}$$

At times $t > t^*$, no further damage occurs, and tissue reaction initiates in terms of inflammatory pathways. The latter exhibit characteristic times $t^*_{\mathrm{react}} \gg t^*$.

It is considered that the inflammatory phase aims to replace damaged collagen with new one. In this case, mass changes, both addition and depletion, are admitted, resulting in $\dot{\rho}^{\mathrm{c}}_{0_j} \neq 0$. By splitting the total reference mass density of collagen into damaged $\rho^{\mathrm{cd}}_{0_j}$ and intact $\rho^{\mathrm{ci}}_{0_j}$ densities of each fiber family,

$$\rho^{\mathrm{c}}_0(\mathbf{X}, t) = \sum_{j=1}^{4}\rho^{\mathrm{c}}_{0_j}(\mathbf{X}, t) = \sum_{j=1}^{4}\rho^{\mathrm{ci}}_{0_j}(\mathbf{X}, t) + \sum_{j=1}^{4}\rho^{\mathrm{cd}}_{0_j}(\mathbf{X}, t)\,, \quad \forall\, t\,, \tag{5}$$

the damage-related turnover of constituents driven by inflammation is described through functions f_{dam} and f_{int} (see Section 2.4), in turn depending on the chemo-biological state $\mathcal{S}_{\mathrm{cb}}$ (obtained as described in Section 2.3), i.e.

$$\dot{\rho}^{\mathrm{cd}}_{0_j} = f_{\mathrm{dam}}(\mathcal{S}_{\mathrm{cb}})\,, \quad \text{for } t \geq t^* \quad \text{with } \rho^{\mathrm{cd}}_{0_j}(\mathbf{X}, t^*) = \rho^{\mathrm{cd}*}_{0_j}(\mathbf{X})\,, \tag{6a}$$

$$\dot{\rho}^{\mathrm{ci}}_{0_j} = f_{\mathrm{int}}(\mathcal{S}_{\mathrm{cb}})\,, \quad \text{for } t \geq t^* \quad \text{with } \rho^{\mathrm{ci}}_{0_j}(\mathbf{X}, t^*) = \rho^{\mathrm{ci}*}_{0_j}(\mathbf{X})\,. \tag{6b}$$

2.3. Chemo-biological model

This section defines the molecular and cell species considered in the chemo-biological state $\mathcal{S}_{\mathrm{cb}}$ associated with tissue inflammatory mechanisms, as well as the governing evolution equations. Two molecular species are introduced: the matrix metalloproteinases (MMPs, denoted by M) and the growth factors (GFs, denoted by G), like transforming growth factors-beta (TGF-βs). In addition, four cell types are considered:

1. smooth muscle cells (SMC), both contractile (cSMC or cS) and synthetic (sSMC or sS);
2. quiescent fibroblasts (qF) and their inflammatory phenotypes, collectively referred to as myofibroblasts (mF).

Phenotypes cS and qF are considered to be quiescent and responsible for the basal ECM production and maintenance, while sS and mF are endowed with high synthetic and proliferative characteristics. These are activated during inflammation.

Cell and molecular species are measured in terms of their number concentration $C_{\mathrm{i}} = C_{\mathrm{i}}(\mathbf{X}, t)$ in the reference configuration. The mass balance of each molecular and cell species is governed by transport equations of the form:

$$\dot{C}_{\mathrm{i}} = -\nabla_{\mathbf{X}}\cdot\mathbf{J}_{\mathrm{i}} + P_{\mathrm{i}} - S_{\mathrm{i}}\,, \qquad \mathrm{i} = \mathrm{G}, \mathrm{M}, \mathrm{cS}, \mathrm{sS}, \mathrm{qF}, \text{ and } \mathrm{mF}\,, \tag{7}$$

Table 1
Specific expressions of the fundamental terms in Eqs. (8) governing the mass balance (7) of each molecular and cell species in the chemo-biological model. See Gierig et al. (2023) for further details. Acronyms: GFs, growth factors; MMPs, matrix metalloproteinases; cSMCs, contractile smooth muscle cells; sSMCs, synthetic smooth muscle cells.

Molecules/cells (i)	Flux ($\mathbf{J}_{\mathrm{i}}$)	Production (P_{i})	Sink (S_{i})
GFs (G)	$\mathbf{J}^{\mathrm{diff}}_{\mathrm{G}}$	$P_{\mathrm{S}\to\mathrm{G}}$	$S^{\mathrm{dec}}_{\mathrm{G}}$
MMPs (M)	$\mathbf{J}^{\mathrm{diff}}_{\mathrm{M}}$	$P_{\mathrm{S}\to\mathrm{M}}$	$S^{\mathrm{dec}}_{\mathrm{M}}$
cSMCs (cS)	$\mathbf{0}$	$P^{\mathrm{s}\to\mathrm{q}}_{\mathrm{sS}\to\mathrm{cS}} + P^{\mathrm{s}\to\mathrm{q}}_{\mathrm{mF}\to\mathrm{cS}}$	$P^{\mathrm{q}\to\mathrm{s}}_{\mathrm{cS}\to\mathrm{sS}}\left\langle 1 - \frac{C^{\min}_{\mathrm{cS}}}{C_{\mathrm{cS}}}\right\rangle$
sSMCs (sS)	$\mathbf{J}^{\mathrm{diff}}_{\mathrm{sS}} + \mathbf{J}^{\mathrm{adv}}_{\mathrm{sS}\to\mathrm{G}}$	$S_{\mathrm{cS}} + P_{\mathrm{G}\to\mathrm{sS}}$	$P^{\mathrm{s}\to\mathrm{q}}_{\mathrm{sS}\to\mathrm{cS}} + S^{\mathrm{dec}}_{\mathrm{sS}}$
Fibroblasts (qF)	$\mathbf{J}^{\mathrm{diff}}_{\mathrm{qF}} + \mathbf{J}^{\mathrm{adv}}_{\mathrm{qF}\to\mathrm{G}}$	$P^{\mathrm{bas}}_{\mathrm{qF}}$	$P^{\mathrm{q}\to\mathrm{s}}_{\mathrm{qF}\to\mathrm{mF}} + S^{\mathrm{dec}}_{\mathrm{qF}}$
Myofibroblasts (mF)	$\mathbf{J}^{\mathrm{diff}}_{\mathrm{mF}} + \mathbf{J}^{\mathrm{adv}}_{\mathrm{mF}\to\mathrm{G}}$	$P^{\mathrm{q}\to\mathrm{s}}_{\mathrm{qF}\to\mathrm{mF}} + P_{\mathrm{G}\to\mathrm{mF}}$	$P^{\mathrm{s}\to\mathrm{q}}_{\mathrm{mF}\to\mathrm{cS}} + S^{\mathrm{dec}}_{\mathrm{mF}}$

where the flux term $\mathbf{J}_{\mathrm{i}}$, the production term P_{i} and the sink term S_{i} of each molecular and cellular species are given in Table 1. These are defined through the following fundamental terms:

$$\mathbf{J}^{\mathrm{diff}}_{\mathrm{i}} = -D_{\mathrm{i}}\, J\, \mathbf{C}^{-1}\nabla_{\mathbf{X}}C_{\mathrm{i}}\,, \qquad \mathbf{J}^{\mathrm{adv}}_{\mathrm{i}\to\mathrm{G}} = A_{\mathrm{i}\to\mathrm{G}}\, C_{\mathrm{i}}\, \mathbf{C}^{-1}\nabla_{\mathbf{X}}C_{\mathrm{G}}\,, \tag{8a}$$

$$P^{\mathrm{bas}}_{\mathrm{i}} = K_{\mathrm{i}}\langle C_{\mathrm{i}_o} - C_{\mathrm{i}}\rangle\,, \qquad S^{\mathrm{dec}}_{\mathrm{i}} = \eta_{\mathrm{i}}\left\langle C_{\mathrm{i}} - C_{\mathrm{i}_o}\right\rangle\,, \tag{8b}$$

$$P_{\mathrm{S}\to\mathrm{i}} = K_{\mathrm{S}\to\mathrm{i}}C_{\mathrm{S}}\rho^{\mathrm{cd}}_0/\bar{\rho}^{\mathrm{c}}_0\,, \qquad P_{\mathrm{G}\to\mathrm{i}} = K_{\mathrm{G}\to\mathrm{i}}\left\langle C_{\mathrm{G}} - C_{\mathrm{G}_o}\right\rangle\langle\rho^{\mathrm{cd}*}_0\rangle\,, \tag{8c}$$

$$P^{\mathrm{s}\to\mathrm{q}}_{\mathrm{j}\to\mathrm{i}} = R_{\mathrm{j}\to\mathrm{i}}\, C_{\mathrm{i}}\, E_{\mathrm{s}\to\mathrm{q}}(\rho^{\mathrm{c}}_0)\,, \qquad P^{\mathrm{q}\to\mathrm{s}}_{\mathrm{j}\to\mathrm{i}} = R_{\mathrm{j}\to\mathrm{i}}\, C_{\mathrm{i}}\, E_{\mathrm{q}\to\mathrm{s}}(\rho^{\mathrm{c}}_0)\,, \tag{8d}$$

representing diffusive $\mathbf{J}^{\mathrm{diff}}_{\mathrm{i}}$ and convective $\mathbf{J}^{\mathrm{adv}}_{\mathrm{i}\to\mathrm{G}}$ fluxes (the latter driven by growth factors' distributions); basal production $P^{\mathrm{bas}}_{\mathrm{i}}$ and natural decay or apoptosis terms $S^{\mathrm{dec}}_{\mathrm{i}}$; molecular overproduction terms from synthetic cells $P_{\mathrm{S}\to\mathrm{i}}$; cell proliferative terms due to growth factors (above a threshold concentration C_{G_o}) in the presence of damage $P_{\mathrm{G}\to\mathrm{i}}$; and synthetic-to-quiescent $P^{\mathrm{s}\to\mathrm{q}}_{\mathrm{j}\to\mathrm{i}}$ or quiescent-to-synthetic $P^{\mathrm{q}\to\mathrm{s}}_{\mathrm{j}\to\mathrm{i}}$ cell switch terms. The latter are respectively governed via switch functions $E_{\mathrm{s}\to\mathrm{q}}$ (from synthetic to quiescent phenotype) and $E_{\mathrm{q}\to\mathrm{s}}$ (viceversa) that describe the effect of ECM micro-environment in the modulation of SMCs phenotypes:

$$E_{\mathrm{s}\to\mathrm{q}}\left(\rho^{\mathrm{c}}_0\right) = 1 - \exp\left[-\left\langle\frac{\rho^{\mathrm{c}}_0}{\bar{\rho}^{\mathrm{c}}_0} - 1\right\rangle\right]\,, \quad E_{\mathrm{q}\to\mathrm{s}}\left(\rho^{\mathrm{c}}_0\right) = 1 - \exp\left[-\left\langle\frac{\bar{\rho}^{\mathrm{c}}_0}{\rho^{\mathrm{c}}_0} - 1\right\rangle\right]\,. \tag{9}$$

These functions enable the regulation of phenotype switching based on the collagen amount ρ^{c}_0 with respect to a reference homeostatic level $\bar{\rho}^{\mathrm{c}}_0$.

2.4. Turnover of constituents

This section defines the evolution laws f_{dam} and f_{int}, governing respectively the degradation of damaged collagen and the production of new one. Firstly, a density-based weighted damage variable computed at the end of the damaging phase, denoted as $\tilde{d}^*_j$, is introduced for each fiber family:

$$\tilde{d}^*_j = \left.\frac{\rho^{\mathrm{c}}_{0_j}}{\rho^{\mathrm{c}}_0}\, d_j\right|_{t=t^*}\,. \tag{10}$$

This variable accounts for the fact that damage in a fiber family with higher density has a more substantial impact on tissue mechanics. Assuming that the replacement of damaged fibers is prioritized based on their functional role in the tissue, the turnover of collagen related to damage is governed by $\tilde{d}^*_j$. From Eq. (10), a total collagen damage measure $d^* = \sum_{j=1}^{4}\tilde{d}^*_j$ can be also computed.

The degradation of damaged collagen fiber families is given by:

$$\dot{\rho}^{\mathrm{cd}}_{0_j} = \frac{\tilde{d}^*_j}{d^*}\dot{\rho}^{\mathrm{cd}}_0 \quad \text{for } t > t^* \text{ with } \rho^{\mathrm{cd}}_{0_j}(\mathbf{X}, t^*) = \rho^{\mathrm{cd}*}_{0_j}(\mathbf{X})\,, \tag{11}$$

Table 2
Vessel geometrical parameters in the reference configuration and initial tissue composition (i.e., values $\bar{f}$ of quantity f at time $t = 0$), together with relevant sources.

Parameter	*Symbol*	*Value*	*Unit*	*Source*
Vessel geometry (reference configuration)				
Vessel internal radius	r_i	1.21	mm	Holzapfel et al. (2005)[a]
Adventitia thickness	t_{A}	0.29	mm	Holzapfel et al. (2005)[a]
Media thickness	t_{M}	0.41	mm	Holzapfel et al. (2005)[a]
Stenotic internal radius	$r_{\mathrm{i}}^{\mathrm{Pl}}$	0.89	mm	Holzapfel et al. (2005)[a]
Stenotic adventitia thickness	$t_{\mathrm{A}}^{\mathrm{Pl}}$	0.32	mm	Holzapfel et al. (2005)[a]
Stenotic media thickness	$t_{\mathrm{M}}^{\mathrm{Pl}}$	0.69	mm	Holzapfel et al. (2005)[a]
Vessel segment length	ℓ	14	mm	–
Stenosis length	ℓ_{Pl}	8.83	mm	–
Media layer (chemo-mechano-biological model)				
Tissue density	$\bar{\rho}_0 = \bar{\rho}$	1	mg/mm^3	Wilson et al. (2012)
Total collagen density	$\bar{\rho}_0^{\mathrm{c}}$	$0.46\bar{\rho}$	mg/mm^3	Chen and Kassab (2017)
Fiber family density	$\bar{\rho}_{0\phi}^{\mathrm{c}}$	$0.69\bar{\rho}_0^{\mathrm{c}}$	mg/mm^3	fitted[b]
	$\bar{\rho}_{0z}^{\mathrm{c}}$	$0.21\bar{\rho}_0^{\mathrm{c}}$	mg/mm^3	fitted[b]
Growth factors (GFs)	$\bar{C}_{\mathrm{G}}$	35	pg/mm^3	Schaan et al. (2007)
Matrix metalloproteinases (MMPs)	$\bar{C}_{\mathrm{M}}$	56	pg/mm^3	Laviades et al. (1998)
Contractile SMCs	$\bar{C}_{\mathrm{cS}}$	4.5	10^4 cell/mm^3	Tracy (1997)
Synthetic SMCs	$\bar{C}_{\mathrm{sS}}$	0	10^4 cell/mm^3	Schwartz et al. (1986)
Fibroblasts (qF)	$\bar{C}_{\mathrm{qF}}$	0	10^4 cell/mm^3	Forte et al. (2010)
Myofibroblasts (mF)	$\bar{C}_{\mathrm{mF}}$	0	10^4 cell/mm^3	Forte et al. (2010)
Adventitia layer (mechanical model)				
Tissue density	$\bar{\rho}_0 = \bar{\rho}$	1	mg/mm^3	Wilson et al. (2012)
Total collagen density	$\bar{\rho}_0^{\mathrm{c}}$	$0.6\bar{\rho}$	mg/mm^3	Chen and Kassab (2017)
Fiber family density	$\bar{\rho}_{0\phi}^{\mathrm{c}}$	$0.1\bar{\rho}_0^{\mathrm{c}}$	mg/mm^3	fitted[b]
	$\bar{\rho}_{0z}^{\mathrm{c}}$	$0.8\bar{\rho}_0^{\mathrm{c}}$	mg/mm^3	fitted[b]

[a] Adapted.
[b] Based on data by Holzapfel et al. (2005).

where $\dot{\rho}_0^{\mathrm{cd}}$ is the collective degradation of damaged collagen due to MMPs, defined as:

$$\dot{\rho}_0^{\mathrm{cd}} = -\eta_{\mathrm{d1}}^{\mathrm{c}} \left[1 - \exp\left(-\eta_{\mathrm{d2}}^{\mathrm{c}} \left\langle \frac{C_{\mathrm{M}} - C_{\mathrm{M}_o}}{C_{\mathrm{M}_o}} \right\rangle \right) \right] . \tag{12}$$

Eq. (12) describes collagen degradation starting as soon as the threshold concentration C_{M_o} is exceeded, with a rate depending on $\eta_{\mathrm{d2}}^{\mathrm{c}}$ but limited by $\eta_{\mathrm{d1}}^{\mathrm{c}}$ when $C_{\mathrm{M}} \gg C_{\mathrm{M}_o}$.

New collagen is produced along the direction of higher damage, and then higher degradation (cf. Eq. (11)), through:

$$\dot{\rho}_{0_j}^{\mathrm{ci}} = \frac{\tilde{d}_j^*}{d^*} \dot{\rho}_0^{\mathrm{ci}} \quad \text{for } t > t^* \text{ with } \rho_{0_j}^{\mathrm{ci}}(\mathbf{X}, t^*) = \rho_{0_j}^{\mathrm{ci}*}(\mathbf{X}) . \tag{13}$$

Here, $\dot{\rho}_0^{\mathrm{ci}}$ is a collective production of intact collagen from synthetic SMCs and myofibroblasts, described as:

$$\dot{\rho}_0^{\mathrm{ci}} = K_{\mathrm{p}}^{\mathrm{c}} \left(C_{\mathrm{sS}} + C_{\mathrm{mF}} \right) \left\langle 1 - \frac{\rho_0^{\mathrm{c}}}{\rho_0^{\mathrm{c},max}} \right\rangle , \tag{14}$$

where $K_{\mathrm{p}}^{\mathrm{c}}$ modulates collagen production by synthetic cells. The term in the Macaulay brackets prevents unlimited collagen production, limited by $\rho_0^{\mathrm{c},max}$.

2.5. Chemo-biology driven growth

Growth is regarded as a source of elastic swelling by considering a constant spatial tissue density: $\rho = \bar{\rho} = const$, (Braeu et al., 2019). This condition is known as incompressible growth and corresponds to volume changes equal to:

$$J(\mathbf{X}, t) = \rho_0(\mathbf{X}, t)/\bar{\rho} . \tag{15}$$

The reference tissue density is computed from single tissue constituents as:

$$\rho_0 = \rho_0^{\mathrm{c}} + \rho_0^{\mathrm{m}} + \alpha_{\mathrm{S}}(C_{\mathrm{cS}} + C_{\mathrm{sS}}) + \alpha_{\mathrm{qF}} C_{\mathrm{qF}} + \alpha_{\mathrm{mF}} C_{\mathrm{mF}} , \tag{16}$$

where α_{i} is the average mass of single cells, here chosen the same for all species as $\alpha = 10\,\mathrm{ng/cell}$. Molecular species are neglected since their mass is more than six-order of magnitudes smaller than ECM constituents and cells.

Since cell concentrations follow the mass balance in Section 2.3 and collagen density undergoes turnover as described in Section 2.4, tissue density varies in time and space. Thus, chemo-biological mechanisms translates into an overall volume change of the tissue via Eq. (15).

As discussed by Gierig et al. (2023), growth is treated from the computational viewpoint as an internal material constraint on volume change via a penalty approach with bulk constant κ. In this way, the direction of growth is not decided *a priori*, but determined via minimization of the potential energy, thus favoring the most compliant directions.

2.6. Case study

The model is employed to simulate balloon angioplasty in a human stenosed coronary artery segment and its subsequent effects on damage and vessel remodeling. The artery is treated as a two-layered structure, where no plaque is considered. The inner layer comprises both media and intima. Its response is governed by the full chemo-mechano-biological model. The outer layer represents the adventitia, serving as a supportive structure to reproduce the overall vessel's mechanical response under pressure. Hence, only elasto-plastic and remodeling mechanisms are considered, without the coupling with chemo-biology. The surrounding fatty or muscular tissue constraining the outward expansion of coronary arteries is considered via linear spring elements applied in the radial direction at the outer surface of the artery. The only cell species that originates in the adventitia are fibroblasts, whose flux from the adventitia into the media is considered proportional to the difference between C_{G} at the boundary and a threshold value C_{G_o} with proportionality constant k_{qF}.

2.6.1. Simulation steps

The simulation of a balloon angioplasty procedure is divided into four steps, where the chemo-biological model is active only in the fourth step.

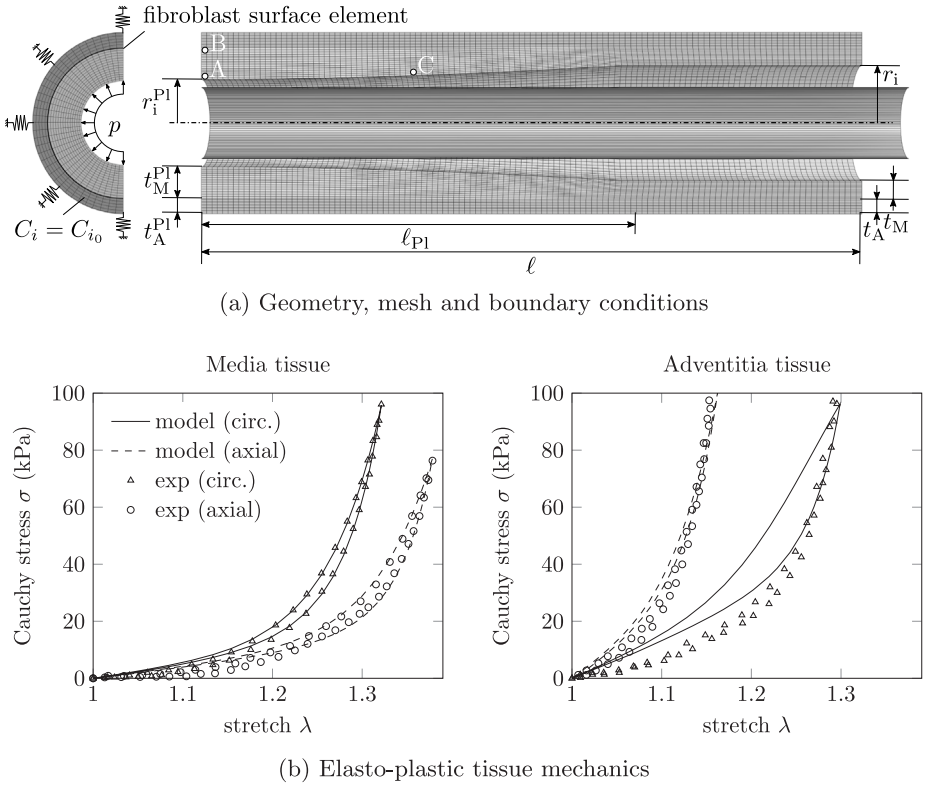

Fig. 2. Simulation settings for the balloon angioplasty of a coronary artery. (a) Geometry, computational mesh, loads and boundary conditions. The figure shows the *in vivo* artery configuration, corresponding to the end of step 2 introduced in Section 2.6. Assuming rotational symmetry and symmetry with respect to the axial direction at the left hand side (at the narrowest lumen), only $^1/_8$-th of the geometry is modeled and symmetry boundary conditions are properly applied. (b) Model tissue elasto-plastic response compared with experimental data by Holzapfel et al. (2005) from uniaxial traction tests.

1. To account for prestretch, a first preliminary simulation step is conducted in which the artery is stretched by 2 mm in axial direction and a mean physiological blood pressure of 13 kPa ≈ 100 mmHg is imposed at the inner surface. Only elastic deformations are considered.
2. In a second preliminary step, axial stretch and inner pressure are held constant. Changes in both elastic and remodeling deformations are considered, but no damage/plasticity.
3. In the third step, a balloon is expanded in the lumen, then deflated and removed. Inflation and deflation are simulated, each lasting one minute, by employing a time-dependent displacement boundary condition applied to the balloon that linearly varies over time. If not differently specified, the maximum balloon expansion results in $u_b = 0.33 r_i^{Pl}$. Both elastic and plastic deformations occur in this phase. Given its brief duration, any homeostasis-driven remodeling is negligible.
4. In the last simulation step, vessel remodeling is monitored for a duration of 1 year. Hence, the full chemo-mechano-biological model is considered.

The *in vivo* arterial configuration, obtained at the end of step 2, is shown in Fig. 2(a), where geometrical parameters are defined as listed in Table 2. Therein, also initial tissue conditions are detailed. Mass densities of single tissue constituents are chosen, together with elasto-plastic parameters, to reproduce the passive behavior of coronary arterial tissues as obtained by Holzapfel et al. (2005) (see Fig. 2(b)). Values of elasto-plastic parameters are given in Table 3, where also parameters governing growth and remodeling are listed. Finally, reference values of chemo-biological parameters are provided in Table 4. They refer to a normoplastic condition, indicating the maintenance of normal physiological functions and structure without excessive proliferation or atrophy (Gierig, 2022; Gierig et al., 2021, 2023). Values in Table 4 are associated with the reference case study of present study, labeled as *ref*. The effects of their variations will be investigated in a dedicated parametric study.

2.6.2. Numerical model

Simulations are implemented by means of the finite element software Abaqus through a user-defined routine developed through the Wolfram Mathematica package AceGen (Korelc and Wriggers, 2016). A detailed explanation of the employed finite element formulations is given by Gierig et al. (2023), while implementation details can be found in Gierig (2022). Briefly, primary variables represent displacements and molecular or cell concentrations, apart from the concentration of contractile SMCs that are local (material-point level) history variables together with plastic and remodeling stretches, as well as damaged and intact collagen densities. The mesh consists of hexahedral elements with linear interpolation for the primary variables. A mixed variational functional to avoid locking due to incompressible growth is implemented, with element-wise constant scalar Lagrange multipliers for pressure and volume dilation. These latter are statically condensed at element level. Since tissue remodeling is assumed to take place mainly in the media, the finite element formulation in the adventitia is purely mechanical (i.e., based only on displacements as primary variables, and on damage, plastic and remodeling variables as history ones). Fibroblast flux from the adventitia and the balloon are treated through 4-noded quadrilateral flux surface elements, and 4-noded quadrilateral surface elements. The contact between artery and balloon is modeled via a surface-to-surface contact formulation, where the balloon is the master surface and the inner arterial surface the slave one. Contact is

Table 3
Values of parameters governing the elasto-plastic and growth and remodeling response, together with relevant sources.

Parameter	*Symbol*	*Value*	*Unit*	*Source*
Media layer elasto-plastic mechanics				
Matrix stiffness modulus	μ	100	N mm/g	fitted[a]
Fiber stiffness modulus	k_1	9.18	N mm/g	fitted[a]
Fiber stiffening parameter	k_2	5.30	–	fitted[a]
Fiber plastic threshold	$\bar{\lambda}_p$	1.18	–	fitted[a]
Fiber damage slope	m_p	2.0	–	fitted[a]
Adventitia layer elasto-plastic mechanics				
Matrix stiffness modulus	μ	100	N mm/g	fitted[a]
Fiber stiffness modulus	k_1	52.19	N mm/g	fitted[a]
Fiber stiffening parameter	k_2	11.15	–	fitted[a]
Fiber plastic threshold	$\bar{\lambda}_p$	1.10	–	fitted[a]
Fiber damage slope	m_p	3.88	–	fitted[a]
Growth and remodeling				
Fiber preferred stretch	λ^c_{pre}	1.062	–	Cyron and Humphrey (2017)
Fiber remodeling rate	k_r	0.8	1/year	fixed
Growth penalty parameter	κ	10^5	N mm/g	calibrated

[a] Based on data by Holzapfel et al. (2005).

treated with a linear pressure-overclosure relationship measured along the normal direction. As regards the outer spring stiffness, a value of 2.5 kN/mm is chosen such that the outer vessel radius only marginally changes during the healing phase.

Information regarding general simulation settings and boundary conditions can be found in Fig. 2(a). A mesh sensitivity analysis determined that our models required approximately 45.000 finite elements for the artery and balloon, along with approximately 8.000 contact elements between balloon and artery. Mesh convergence was confirmed by conducting simulations with finer meshes (up to 2× elements), which resulted in differences less than 5% in the model's outcomes of interest (species concentrations, masses, volumetric growth). A complete simulation process takes approximately 16 h using the direct solver with 6 processors (Intel Core i7-7700 CPU @ 3.6 GHz, 32 GB Memory).

3. Results

Results from steps 3 and 4 introduced in Section 2.6.1 are discussed in Sections 3.1 and 3.2, respectively. A parametric study is discussed in Section 3.3, while comparisons to human data in Section 3.4.

3.1. Balloon expansion

Due to balloon expansion, the arterial tissue undergoes damage, and the proposed modeling framework quantifies the amount of elastoplastic damage in collagen fibers within the arterial wall. Figs. 3(a) and 3(b) show the amount of damaged and intact collagen just after angioplasty. Higher damage occurs where the stenosis is more pronounced. Additionally, collagen damage is highest toward the inner surface of the artery, with maximum value $d^*_{max} = 0.37$, and diminishes in the radial direction. In non-stenosed areas, the obtained collagen damage is null.

3.2. Post-angioplasty tissue growth and remodeling dynamics

Tissue composition after 1 year post-angioplasty, which arise from growth and remodeling mechanisms driven by chemo-biology, results highly inhomogeneous. Changes in species concentrations and collagen production at points A, B, and C (cf., Fig. 2(a)) are shown in Fig. 4. Point A, situated in the most stenotic lumen region, experiences the highest damage. Point B also lies within the stenotic region, positioned at the media-adventitia border, yet it remains undamaged. Point C, positioned at the onset of the stenosis on the lumen side, exhibits lower damage compared to point A.

Significant tissue remodeling occurs within the initial weeks post-balloon angioplasty, stabilizing between three months to a year. Notably, remodeling is most pronounced at position A, experiencing the highest damage, followed by point C, where the vessel is less affected. At point B, where the tissue remains intact, remodeling is minimal. Here, changes in cell and molecular concentrations result solely from species transport. Additionally, contractile SMCs do not change their phenotype due to the absence of damaged collagen. In contrast, at points A and C, the concentrations of collagen and contractile SMCs initially decrease and then rise: collagen is degraded by MMPs, while GFs induce the switch of cSMC into sSMC, which in turn produce new collagen. It is worth pointing out that a different trend is observed for fibroblasts. As they migrate from the adventitia into the media, their concentration peaks at point B, similar to point A. Conversely, due to lower presence of GFs at point C, only a few cells migrate there.

The final collagen concentration after one year shows minimal increase compared to pre-angioplasty levels. Similarly, contractile SMCs revert nearly to their initial values after transitioning to a synthetic phenotype within the initial 100 days.

3.3. Parametric study

The predicted vessel remodeling obtained with the reference case study *ref* is now compared in Fig. 4 with the one obtained with different values of chemo-biological parameters. As detailed in Table 5, the different case studies are characterized by:

1. *cell syn* $N\times$ – synthetic cell overproduction via $N\times$ increase of phenotypic modulation and GF-mediated proliferation;
2. *col syn* 2× – increased collagen synthesis from synthetic cells.

The evolution of GFs and MMPs remains analogous across all cases since damage is identical and parameters governing molecular dynamics are not varied. However, cell species show in general heightened responsiveness compared to the reference example, resulting in increased final concentrations of contractile SMCs and collagen in all simulation cases.

Collagen concentration significantly responds to increased collagen synthesis, while the final concentration of contractile SMCs is highly sensitive to synthetic cell overproduction. For instance, at point A, the *cell syn* 2× case exhibits a 6% increase, and the *cell syn* 4× case shows a 20% rise in final contractile SMC concentration, indicating the nonlinear nature of this process. The final distribution of contractile SMCs obtained after a 1-year follow-up for the *cell syn* 4× case study is illustrated in Fig. 3(c). It is noteworthy that the altered cell distribution induces high heterogeneities in ECM composition, as depicted for collagen in Fig. 3(d).

Fibroblast concentration remains stable at point B due to consistent GF levels across all cases. However, at points A and C, variations occur due to fibroblast transitions to myofibroblasts, particularly notable at point A. Enhanced phenotypic modulation (*cell syn* 2× and 4× cases) decreases fibroblast content near the lumen, whereas accelerated collagen production (*col syn* 2× case) reduces the stimulus for phenotype transition, resulting in increased fibroblast accumulation.

3.4. Comparison to human restenosis data

The simulation results are compared with clinical data by Nobuyoshi et al. (1988). To mitigate the effects of post-treatment tissue viscoelastic recoil, unaccounted for in the *in silico* model, both clinical data and model predictions are normalized concerning the vessel radius at day 1. Specifically, model predictions showcase the normalized radius at the narrowest site (point A in Fig. 2(a)). The comparison between *in silico* results and clinical data is illustrated in Fig. 5, where different case studies are addressed such to highlight the role of different chemo-mechano-biological mechanisms on vessel remodeling (i.e., lumen enlargement or decrease).

Table 4
Values of parameters for the chemo-biological model, together with relevant sources. The present set of values refers to the reference case study (*ref*).

Parameter	*Symbol*	*Value*	*Unit*	*Source*
		Matrix Metalloproteinases (MMPs)		
Diffusion constant	D_M	1	$\mu m^2/s$	Collier and Goldberg (2015)
Production rate from SMCs	$K_{S\to M}$	0.05	pg/(cell month)	Escuer et al. (2019)
Natural decay	η_M	0.2	1/day	Boyle et al. (2011)
Threshold concentration	C_{M_o}	56	$pg/\mu m^3$	$\bar{C}_M$
		Growth Factors (GFs)		
Diffusion constant	D_G	1	$\mu m^2/s$	Levine et al. (2001)
Production rate from SMCs	$K_{S\to G}$	0.02	pg/(cell month)	$K_{S\to M}$
Natural decay	η_G	0.01	1/day	Boyle et al. (2011)
Threshold concentration	C_{G_o}	35	$pg/\mu m^3$	$\bar{C}_G$
		Contractile (cS) and synthetic (sS) smooth muscle cells		
Diffusion constant	D_{sS}	70	$\mu m^2/h$	Escuer et al. (2019)[a]
Conversion rate (cS to sS)	$R_{cS\to sS}$	0.04	1/day	Escuer et al. (2019)[a]
Conversion rate (sS to cS)	$R_{sS\to cS}$	0.20	1/day	Escuer et al. (2019)[a]
Conversion rate (mF to cS)	$R_{mF\to cS}$	0.20	1/day	$R_{sS\to cS}$
Chemotactic constant (sS to GF)	$A_{sS\to G}$	3	$mm^5/(ng\,day)$	estimated
Production rate from GFs (sS)	$K_{G\to sS}$	0.25	cell/(ng s)	Escuer et al. (2019)
Apoptotic rate (sS)	η_{sS}	0.01	1/year	Escuer et al. (2019)
Threshold concentration (sS)	C_{sS_o}	0	10^4 cell/mm^3	$\bar{C}_{sS}$
Minimum concentration (cS)	$\bar{C}_{cS}^{min}$	$0.7\bar{C}_{cS}$	10^4 cell/mm^3	fixed
		Fibroblasts (qF) and Myofibroblasts (mF)		
Diffusion constant (qF)	D_{qF}	430	$\mu m^2/h$	Koppenol et al. (2017)[a]
Diffusion constant (mF)	D_{mF}	540	$\mu m^2/h$	Pot et al. (2010)[a]
Chemotactic constant (qF to GF)	$A_{qF\to G}$	17	$mm^5/(ng\,day)$	estimated
Chemotactic constant (mF to GF)	$A_{mF\to G}$	17	$mm^5/(ng\,day)$	$A_{qF\to G}$
Conversion rate (qF to mF)	$R_{qF\to mF}$	0.5	1/day	$R_{sS\to cS}$
Proliferation rate (qF)	K_{qF}	0.04	1/day	η_{qF}
Production rate from GFs (mF)	$K_{G\to mF}$	0.25	cell/(ng s)	$K_{G\to sS}$
Apoptotic rate (qF)	η_{qF}	0.04	1/day	Olsen et al. (1995)
Threshold concentration (qF)	C_{qF_o}	0	10^4 cell/mm^3	$\bar{C}_{qF}$
Apoptotic rate (mF)	η_{mF}	0.03	1/day	Koppenol et al. (2017)
Threshold concentration (mF)	C_{mF_o}	0	10^4 cell/mm^3	$\bar{C}_{mF}$
Flux constant (qF)	k_{qF}	0.17	cell µm/(g day)	calibrated
		Collagen turnover		
Collagen production rate	K_p^c	3	ng/(cell day)	Nolan and Lally (2018)[a]
Maximum collagen density	$\rho_0^{c,max}$	$1.5\bar{\rho}_0^c$	mg/mm^3	Escuer et al. (2019)
Collagen degradation constants	η_{d1}^c	1	$\mu g/(mm^3\,h)$	Murphy et al. (2012)[a]
	η_{d2}^c	10	–	Gierig et al. (2021)

[a] A thorough discussion on these values is presented by Gierig (2022) and Gierig et al. (2023).

Table 5
Multiplying factor applied to the reference values of parameters of the chemo-biological model (see Table 4) in the case studies presented in Sections 3.3 and 3.4. In all cases, the apoptotic parameters of cells that are not present under homeostatic conditions (i.e., η_{sS}, η_{qF}, and η_{mF}) are increased by factor five for a faster removal of these cell species.

Case study	K_p^c	η_{d1}^c	$K_{G\to sS}$	$K_{G\to mF}$	$R_{cS\to sS}$	$R_{sS\to cS}$	$R_{mF\to cS}$	$R_{qF\to mF}$
cell syn $N\times$	1	1	N	N	N	N	N	N
col syn 2×	2	1	1	1	1	1	1	1
slow	0.3	0.5	1	1	0.5	0.5	0.5	0.5

The model effectively replicates the observed bimodal temporal dynamics noted in clinical studies (Nobuyoshi et al., 1988; Kimura et al., 1997; Kleber et al., 2015; Ueno et al., 2023), providing valuable insights into its correlation with tissue remodeling (Pasterkamp et al., 2000). The simulation results demonstrate early lumen enlargement in the first weeks after angioplasty, depicted by the increased internal radius in Fig. 5. Figures 4 illustrate the connection between early lumen enlargement and the initial removal of damaged constituents.

Subsequently, the internal radius decreases as new collagen synthesis and SMC proliferation occur, signifying long-term tissue growth mechanisms. The greater increase in tissue thickness is linked to amplified cell proliferation and/or enhanced collagen production. The comparison among the reference case study *ref* with *cell syn* 2×, *cell syn* 4×, and *col syn* 2× explores the relative significance of these mechanisms. Elevated collagen production appears to play a pivotal role in determining the final tissue content. Notably, the *col syn* 2× simulation predicts long-term tissue growth (after 1 year) within the range of available clinical data.

However, the predicted early tissue resorption does not precisely match clinical data, both in values (maximum inner radius) and timing. Clinical records indicate short-term tissue resorption occurring up to the first month post-implantation (around 30 days), while the model's resorption peak occurs within the initial ten days. To better emulate *in vivo* short-term dynamics, an additional parameter set, labeled as *slow* in Table 5, is considered. Here, rates of cell phenotypic switches (from quiescent to synthetic cells and vice versa) are decreased, delaying new collagen production. Slower rates of collagen depletion and production are also considered, enhancing the final amount of contractile SMCs and collagen by reducing collagen removal and increasing initial lumen gain. These adjustments stem from a comprehensive sensitivity study outlined by Gierig (2022).

In this modified scenario, the dynamics of early tissue resorption aligns closely with clinical data in Fig. 5. It demonstrates maximum tissue resorption after 1 month and long-term tissue growth around 3 months post-implantation, maintaining stability up to a 1-year follow-up.

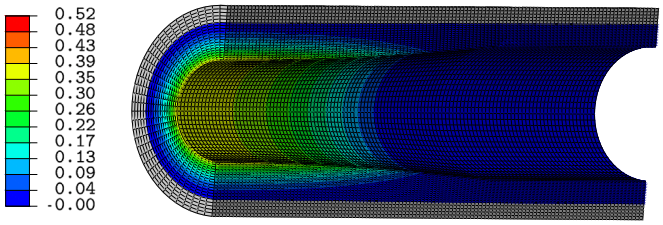

(a) Collagen damage just after balloon angioplasty (d^*).

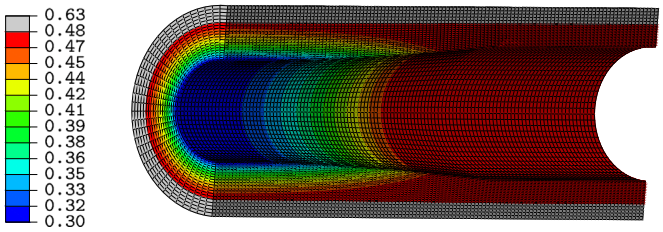

(b) Intact collagen distribution just after balloon angioplasty (ρ_0^{ci} in mg/mm^3).

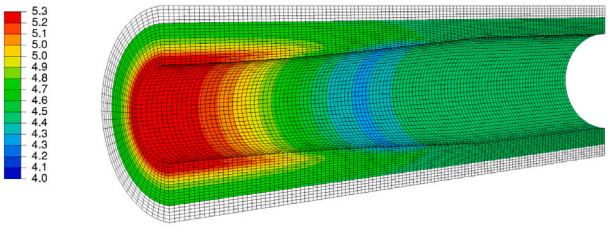

(c) Contractile SMCs distribution 1 year post-angioplasty (C_{cS} in 10^4 cell/mm^3).

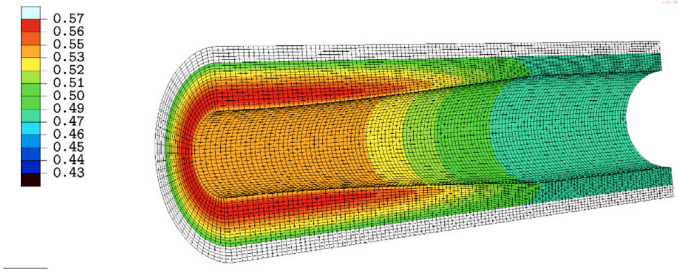

(d) Collagen distribution 1 year post-angioplasty (ρ_0^{c} in mg/mm^3).

Fig. 3. *In silico* tissue growth and remodeling dynamics: balloon expansion induces damage in the vessel (a), reducing the content of intact collagen (b); an inflammatory response is activated, leading to tissue remodeling during a 1-year follow up. This is shown for the *cell syn* 4× case study (see Section 3.3) in terms of contractile SMCs (c) and collagen (d) distributions.

The *slow* case study is also explored with various balloon inflation levels u_{b}, correlating with different post-angioplasty tissue damage distributions. In comparison to the reference case, the balloon expansion is increased by 15%, resulting in a 21% increase in maximum damage ($d \uparrow$ case), and by 30%, leading to a 40% increase in maximum damage ($d \Uparrow$ case). The model illustrates that early tissue resorption during the tissue remodeling phase amplifies with increased damage, as depicted in Fig. 5. Additionally, long-term tissue growth after 1 year increases with higher induced damage. Quantitatively, the trend implies that *in vivo* tissue damage post-angioplasty might surpass the levels replicated by the adopted damage model.

4. Discussions

Numerical simulations confirm our hypothesis that subintimal damage and subsequent tissue remodeling can explain the bimodal dynamics of restenosis. Aligning *in silico* outcomes with clinical data sheds light on tissue damage, collagen synthesis, and cell phenotypes in the post-angioplasty inflammatory response. This study marks an initial step towards an *in silico* tool for retrospective patient-specific assessments of the chemo-mechano-biological mechanisms driving post-angioplasty vessel remodeling.

Compared to available models, the one herein presented addresses the effects of subintimal damage, rather than the widely-explored

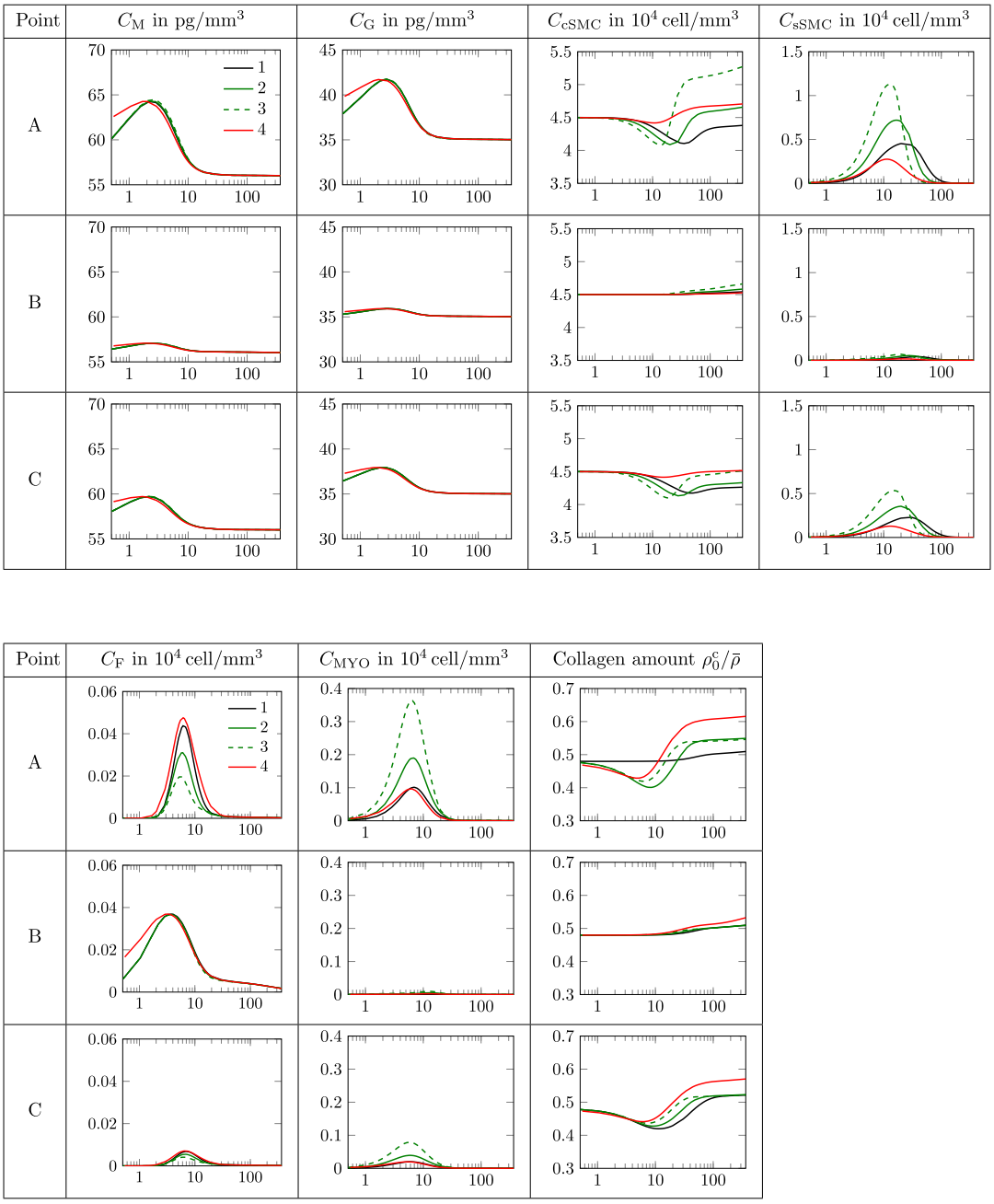

Fig. 4. Comparison of model outcomes with different sets of model parameters in material points A,B, and C (see Fig. 2(a)). Case 1: *ref*; case 2: *cell syn* 2×; case 3: *cell syn* 4×; case 4: *col syn* 2×. Values of parameters listed in Tables 2, 4 and 5. The abscissa represents time in days within the first year post treatment (in log scale).

endothelial one. Furthermore, it incorporates residual stresses in the *in vivo* configuration by achieving a homeostatic state in collagen fibers through remodeling. The latter affects also tissue mechanical response during the inflammatory phase, addressing an issue that is often overlooked in existing models (Escuer et al., 2019; Corti et al., 2021, 2022; Manjunatha et al., 2022; Corti et al., 2023; Manjunatha et al., 2023). Moreover, with respect to state-of-the-art modeling results, the bimodal nature of the lumen area tissue remodeling dynamics is clearly demonstrated, quantitatively reproducing the amount of long-term tissue growth. It also captures trends in early tissue repair mechanisms, although early vessel remodeling is not reproduced in quantitative terms. However, it is important to note the model focuses solely on the inflammatory response triggered by collagen damage due to overstretch. Further effort towards a quantitative comparison with clinical data is not pursued as it may offer limited insights without considering more realistic conditions or additional experimental evidence, as discussed ahead.

In fact, the study is not exempt from limitations. Firstly, the model lacks consideration for viscoelastic recoil, restricting the ability to provide precise predictions within the initial post-treatment period. As regards remodeling, the stretch-based criterion adopted in the model, though evolved from the state-of-the-art, is arbitrary and requires refinement using more mechanobiological insights (Eichinger et al., 2021). Additionally, this criterion leads to numerical instabilities, limiting the achievable degree of simulated stenosis, as shown by Gierig (2022).

Furthermore, the simulations exclude plaques within the internal lumen. Plaque composition is known to affect the incidence of restenosis (Rodriguez-Granillo et al., 2006; He et al., 2019a), since it may have an effect on artery remodeling by altering stresses and strains in

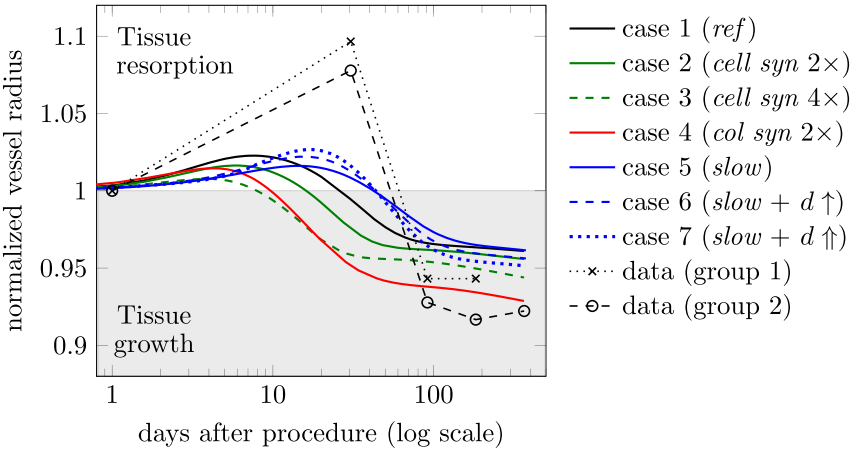

Fig. 5. Evolution of the inner vessel radius at narrowest site (point A in Fig. 2(a)), normalized with respect to the corresponding radius at day 1 after treatment. Comparison between model predictions from different case studies, presented in Sections 3.3 and 3.4, with *in vivo* clinical data by Nobuyoshi et al. (1988).

the vessel and by activating inflammatory pathways (Popa-Fotea et al., 2023; Mastrofini et al., 2024). Plaque-related effects should be included in future studies. Moreover, since changes in plaque area significantly impact lumen area gain *in vivo* (Gil et al., 1996), the simulated lumen gain during angioplasty remains lower than real conditions. A higher level of tissue/plaque stenosis in the simulation would predict increased collagen damage due to greater stretching required for lumen widening. As shown in Fig. 5, higher damage would result in elevated early tissue resorption and long-term tissue growth.

Additionally, damage mechanisms related to non-collagenous constituents (elastin damage or fragmentation of elastic laminae) and their subsequent chemo-biological repair pathways might play a role. New experimental evidence in this regard are needed before models incorporating such mechanisms can be developed. Furthermore, given the significance of phenotypic cell modulation dynamics and collagen production levels in determining the final lumen gain, further experiments are essential to better understand the *in vivo* dynamics of cell activities, especially in relation to genetics or epigenetics factors between different patients. Finally, a comprehensive modeling framework should encompass endothelial denudation that possibly activates surface growth mechanisms on the internal lumen and couples with altered wall shear stresses.

5. Conclusions

This paper introduces a numerical simulation of balloon angioplasty in a stenosed coronary artery using a chemo-mechano-biological model. The model, proposed by Gierig et al. (2023), is based on a continuum framework and captures chemo-mechano-biological inflammatory mechanisms triggered by tissue damage during balloon expansion. By reproducing clinical evidence from human coronary arteries, it validates the hypothesis linking early lumen rearrangement and late restenosis to subintimal damage, early tissue remodeling, and subsequent tissue growth. These findings pave the way for novel therapeutic options targeting these mechanisms (Kakuta et al., 1994; Mintz et al., 1996; Kleber et al., 2015). Moreover, the present simulation framework may be applied in a clinical context as a diagnostic support to identify early time-point criteria for potentially negative outcomes.

Comparing *in silico* predictions with *in vivo* data by Nobuyoshi et al. (1988), adjustments to cell proliferation and collagen production were made to better match experimental outcomes starting from a reference set of parameter values. While the model qualitatively predicts changes in the vessel radius and final re-narrowing after one year, it underestimates early tissue resorption. However, it effectively captures the temporal dynamics of tissue resorption and growth, revealing areas where further experimental data are needed. This study demonstrates the potential of *in silico* analyses in retrospectively understanding patient-specific system biology dynamics, and highlights the need for interdisciplinary efforts towards prospective applications.

CRediT authorship contribution statement

Meike Gierig: Software, Methodology, Investigation, Conceptualization. **Pierfrancesco Gaziano:** Writing – review & editing, Writing – original draft, Visualization. **Peter Wriggers:** Writing – review & editing, Supervision, Resources, Project administration, Funding acquisition. **Michele Marino:** Writing – review & editing, Validation, Supervision, Project administration, Methodology, Conceptualization.

Declaration of competing interest

Each author has been involved in the design of the study, interpretation of the data, and writing of the manuscript.

Each author has read and concurs with the content in the manuscript. The manuscript has not been and will not be submitted for publication elsewhere.

All authors disclose any financial and personal relationships with other people or organizations that could inappropriately influence their work.

Data availability

All data and codes will be made available upon request.

Declaration of Generative AI and AI-assisted technologies in the writing process

During the preparation of this work the authors used ChatGPT in order to enhance the spelling, grammar, and clarity of the abstract and contribution sections. After using this tool, the authors carefully reviewed and edited the content as needed and take full responsibility for the content of the publication.

Acknowledgments

MM and PG gratefully acknowledge funding from Regione Lazio (POR FESR LAZIO 2014; Progetti di Gruppi di Ricerca 2020; project: BIOPMEAT, n. A0375-2020-36756) and support from the Italian National Group for Mathematical Physics GNFM-INdAM. PW gratefully

acknowledges the support by the Deutsche Forschungsgemeinschaft (DFG, German Research Foundation) - SFB/TRR-298-SIIRI - Project-ID 426335750.

References

Balzani, D., Schröder, J., Gross, D., 2006. Simulation of discontinuous damage incorporating residual stresses in circumferentially overstretched atherosclerotic arteries. Acta Biomater. 2 (6), 609–618.

Berridge, M.J., 2012. Cell Signalling Biology. Portland Press, http://dx.doi.org/10.1042//csb0001009.

Boyle, C.J., Lennon, A.B., Prendergast, P.J., 2011. In silico prediction of the mechanobiological response of arterial tissue: application to angioplasty and stenting. J. Biomech. Eng. 133 (8).

Braeu, F.A., Aydin, R.C., Cyron, C.J., 2019. Anisotropic stiffness and tensional homeostasis induce a natural anisotropy of volumetric growth and remodeling in soft biological tissues. Biomech. Model. Mechanobiol. 18 (2), 327–345.

Buganza Tepole, A., Kuhl, E., 2016. Computational modeling of chemo-bio-mechanical coupling: a systems-biology approach toward wound healing. Comput. Methods Biomech. Biomed. Eng. 19 (1), 13–30.

Chen, H., Kassab, G.S., 2017. Microstructure-based constitutive model of coronary artery with active smooth muscle contraction. Sci. Rep. 7 (1), 1–15.

Collier, I.E., Goldberg, G.I., 2015. Dynamics and mechanism of substrate recognition by matrix metalloproteases. Matrix Metalloproteinase Biol. 23–40.

Converse, M.I., Walther, R.G., Ingram, J.T., Li, Y., Yu, S.M., Monson, K.L., 2018. Detection and characterization of molecular-level collagen damage in overstretched cerebral arteries. Acta Biomater. 67, 307–318.

Corti, A., Colombo, M., Migliavacca, F., Berceli, S.A., Casarin, S., Rodriguez Matas, J.F., Chiastra, C., 2022. Multiscale agent-based modeling of restenosis after percutaneous transluminal angioplasty: Effects of tissue damage and hemodynamics on cellular activity. Comput. Biol. Med. 147, 105753. http://dx.doi.org/10.1016/j.compbiomed.2022.105753.

Corti, A., Colombo, M., Migliavacca, F., Matas, J.F.R., Casarin, S., Chiastra, C., 2021. Multiscale computational modeling of vascular adaptation: a systems biology approach using agent-based models. Front. Bioeng. Biotechnol. 9.

Corti, A., Migliavacca, F., Berceli, S.A., Chiastra, C., 2023. Predicting 1-year in-stent restenosis in superficial femoral arteries through multiscale computational modelling. J. R. Soc. Interface 20 (201), 20220876. http://dx.doi.org/10.1098/rsif.2022.0876.

Cyron, C.J., Aydin, R.C., Humphrey, J.D., 2016. A homogenized constrained mixture (and mechanical analog) model for growth and remodeling of soft tissue. Biomech. Model. Mechanobiol. 15 (6), 1389–1403.

Cyron, C.J., Humphrey, J.D., 2017. Growth and remodeling of load-bearing biological soft tissues. Meccanica 52 (3), 645–664.

Davis, C., Fischer, J., Ley, K., Sarembock, I.J., 2003. The role of inflammation in vascular injury and repair. J. Thromb. Haemost. 1 (8), 1699–1709.

Eichinger, J.F., Haeusel, L.J., Paukner, D., Aydin, R.C., Humphrey, J.D., Cyron, C.J., 2021. Mechanical homeostasis in tissue equivalents: a review. Biomech. Model. Mechanobiol. 20 (3), 833–850. http://dx.doi.org/10.1007/s10237-021-01433-9.

Escuer, J., Martínez, M.A., McGinty, S., Peña, E., 2019. Mathematical modelling of the restenosis process after stent implantation. J. R. Soc. Interface 16 (157), 20190313.

Fereidoonnezhad, B., Naghdabadi, R., Sohrabpour, S., Holzapfel, G., 2017. A mechanobiological model for damage-induced growth in arterial tissue with application to in-stent restenosis. J. Mech. Phys. Solids 101, 311–327. http://dx.doi.org/10.1016/j.jmps.2017.01.016.

Forte, A., Della Corte, A., De Feo, M., Cerasuolo, F., Cipollaro, M., 2010. Role of myofibroblasts in vascular remodelling: focus on restenosis and aneurysm. Cardiovasc. Res. 88 (3), 395–405.

Gasser, T.C., Holzapfel, G.A., 2002. A rate-independent elastoplastic constitutive model for biological fiber-reinforced composites at finite strains: continuum basis, algorithmic formulation and finite element implementation. Comput. Mech. 29 (4–5), 340–360.

Gierig, M., 2022. The Mechano-Chemo-Biology of Arterial Growth and Remodeling: A Continuum Modeling Framework for Tissue Response to Damage (Ph.D. thesis). Leibniz University of Hannover.

Gierig, M., Wriggers, P., Marino, M., 2021. Computational model of damage-induced growth in soft biological tissues considering the mechanobiology of healing. Biomech. Model. Mechanobiol. http://dx.doi.org/10.1007/s10237-021-01445-5.

Gierig, M., Wriggers, P., Marino, M., 2023. Arterial tissues and their inflammatory response to collagen damage: A continuum in silico model coupling nonlinear mechanics, molecular pathways, and cell behavior. Comput. Biol. Med. 158, 106811. http://dx.doi.org/10.1016/j.compbiomed.2023.106811.

Gil, R., Di Mario, C., Prati, F., Von Birgelen, C., Ruygrok, P., Roelandt, J.R., Serruys, P.W., Van Swijndregt, W., Ligthart, J., 1996. Influence of plaque composition on mechanisms of percutaneous transluminal coronary balloon angioplasty assessed by ultrasound imaging. Am. Heart J. 131 (3), 591–597.

Glagov, S., Weisenberg, E., Zarins, C., Stankunavicius, R., Kolettis, G., 1987. Compensatory enlargement of human atherosclerotic coronary arteries. New Engl. J. Med. 316 (22), 1371—1375. http://dx.doi.org/10.1056/NEJM198705283162204.

Grytsan, A., Eriksson, T.S.E., Watton, P.N., Gasser, T.C., 2017. Growth description for vessel wall adaptation: A thick-walled mixture model of abdominal aortic aneurysm evolution. Materials 10 (9), 994.

He, H., cheng Weng, J., Zhao, Y., hong Cai, S., ling Zhang, X., hui Yin, H., 2019a. Impact of plaque calcification and stent oversizing on clinical outcomes of atherosclerotic femoropopliteal arterial occlusive disease following stent angioplasty. Eur. J. Vasc. Endovascular Surg. 58 (2), 215–222. http://dx.doi.org/10.1016/j.ejvs.2019.01.025.

He, R., Zhao, L., Silberschmidt, V.V., Liu, Y., 2020. Mechanistic evaluation of long-term in-stent restenosis based on models of tissue damage and growth. Biomech. Model. Mechanobiol. 19 (5), 1425–1446. http://dx.doi.org/10.1007/s10237-019-01279-2.

He, Y., Zuo, D., Hackl, K., Yang, H., Mousavi, S.J., Avril, S., 2019b. Gradient-enhanced continuum models of healing in damaged soft tissues. Biomech. Model. Mechanobiol. 18 (5), 1443–1460.

Holzapfel, G.A., Sommer, G., Gasser, C.T., Regitnig, P., 2005. Determination of layer-specific mechanical properties of human coronary arteries with nonatherosclerotic intimal thickening and related constitutive modeling. Am. J. Physiol.-Heart Circulatory Physiol. 289 (5), H2048–H2058.

Humphrey, J.D., 2013. Cardiovascular Solid Mechanics: Cells, Tissues, and Organs. Springer Science & Business Media.

Humphrey, J.D., Rajagopal, K.R., 2002. A constrained mixture model for growth and remodeling of soft tissues. Math. Models Methods Appl. Sci. 12 (03), 407–430.

Jukema, J.W., Verschuren, J.J.W., Ahmed, T.A.N., Quax, P.H.A., 2012. Restenosis after PCI. Part 1: pathophysiology and risk factors. Nat. Rev. Cardiol. 9 (1), 53–62. http://dx.doi.org/10.1038/nrcardio.2011.132.

Kachanov, L., 1986. Introduction to Continuum Damage Mechanics, vol. 10, Springer Science & Business Media.

Kakuta, T., Currier, J.W., Haudenschild, C.C., Ryan, T.J., Faxon, D.P., 1994. Differences in compensatory vessel enlargement, not intimal formation, account for restenosis after angioplasty in the hypercholesterolemic rabbit model. Circulation 89 (6), 2809–2815. http://dx.doi.org/10.1161/01.CIR.89.6.2809.

Kimura, T., Kaburagi, S., Tamura, T., Yokoi, H., Nakagawa, Y., Yokoi, H., Hamasaki, N., Nosaka, H., Nobuyoshi, M., Mintz, G.S., Popma, J.J., Leon, M.B., 1997. Remodeling of human coronary arteries undergoing coronary angioplasty or atherectomy. Circulation 96 (2), 475–483. http://dx.doi.org/10.1161/01.CIR.96.2.475.

Kleber, F.X., Schulz, A., Köln, P., 2018. Positive vessel remodelling. Eur. Med. J. 3, 111–115.

Kleber, F.X., Schulz, A., Waliszewski, M., Hauschild, T., Böhm, M., Dietz, U., Cremers, B., Scheller, B., Clever, Y.P., 2015. Local paclitaxel induces late lumen enlargement in coronary arteries after balloon angioplasty. Clin. Res. Cardiol. 104 (3), 217–225. http://dx.doi.org/10.1007/s00392-014-0775-2.

Koppenol, D.C., Vermolen, F.J., Niessen, F.B., van Zuijlen, P.P.M., Vuik, K., 2017. A mathematical model for the simulation of the formation and the subsequent regression of hypertrophic scar tissue after dermal wounding. Biomech. Model. Mechanobiol. 16 (1), 15–32.

Korelc, J., Wriggers, P., 2016. Automation of Finite Element Methods. Springer.

Koskinas, K.C., Chatzizisis, Y.S., Antoniadis, A.P., Giannoglou, G.D., 2012. Role of endothelial shear stress in stent restenosis and thrombosis: Pathophysiologic mechanisms and implications for clinical translation. J. Am. Coll. Cardiol. 59 (15), 1337–1349. http://dx.doi.org/10.1016/j.jacc.2011.10.903.

Laviades, C., Varo, N., Fernández, J., Mayor, G., Gil, M.J., Monreal, I., Díez, J., 1998. Abnormalities of the extracellular degradation of collagen type I in essential hypertension. Circulation 98 (6), 535–540.

Levine, H.A., Pamuk, S., Sleeman, B.D., Nilsen-Hamilton, M., 2001. Mathematical modeling of capillary formation and development in tumor angiogenesis: penetration into the stroma. Bull. Math. Biol. 63 (5), 801–863.

Loerakker, S., Ristori, T., 2019. Computational modeling for cardiovascular tissue engineering: the importance of including cell behavior in growth and remodeling algorithms. Curr. Opin. Biomed. Eng.

Maes, L., Cloet, A.-S., Fourneau, I., Famaey, N., 2021. A homogenized constrained mixture model of restenosis and vascular remodelling after balloon angioplasty. J. R. Soc. Interface 18 (178), 20210068. http://dx.doi.org/10.1098/rsif.2021.0068.

Manjunatha, K., Behr, M., Vogt, F., Reese, S., 2022. A multiphysics modeling approach for in-stent restenosis: Theoretical aspects and finite element implementation. Comput. Biol. Med. 150, 106166. http://dx.doi.org/10.1016/j.compbiomed.2022.106166.

Manjunatha, K., Schaaps, N., Behr, M., Vogt, F., Reese, S., 2023. Computational modeling of in-stent restenosis pharmacokinetic and pharmacodynamic evaluation. Comput. Biol. Med. 107686. http://dx.doi.org/10.1016/j.compbiomed.2023.107686.

Marino, M., 2019. Constitutive modeling of soft tissues. In: Narayan, R. (Ed.), Encyclopedia of Biomedical Engineering. Elsevier, Oxford, pp. 81–110. http://dx.doi.org/10.1016/B978-0-12-801238-3.99926-4.

Marino, M., Converse, M.I., Monson, K.L., Wriggers, P., 2019. Molecular-level collagen damage explains softening and failure of arterial tissues: a quantitative interpretation of CHP data with a novel elasto-damage model. J. Mech. Behav. Biomed. Mater. 97, 254–271.

Mastrofini, A., Marino, M., Karlöf, E., Hedin, U., Gasser, T.C., 2024. On the impact of residual strains in the stress analysis of patient-specific atherosclerotic carotid vessels: Predictions based on the homogenous stress hypothesis. Ann. Biomed. Eng. 1–12.

McQueen, A., Escuer, J., Schmidt, A.F., Aggarwal, A., Kennedy, S., McCormick, C., Oldroyd, K., McGinty, S., 2022. An intricate interplay between stent drug dose and release rate dictates arterial restenosis. J. Control. Release 349, 992–1008.

Mintz, G.S., Popma, J.J., Pichard, A.D., Kent, K.M., Satler, L.F., Wong, S.C., Hong, M.K., Kovach, J.A., Leon, M.B., 1996. Arterial remodeling after coronary angioplasty. Circulation 94 (1), 35–43. http://dx.doi.org/10.1161/01.CIR.94.1.35.

Mouw, J.K., Ou, G., Weaver, V.M., 2014. Extracellular matrix assembly: a multiscale deconstruction. Nature Rev. Mol. Cell Biol. 15 (12), 771–785.

Murphy, K.E., Hall, C.L., Maini, P.K., McCue, S.W., McElwain, D.L.S., 2012. A fibrocontractive mechanochemical model of dermal wound closure incorporating realistic growth factor kinetics. Bull. Math. Biol. 74 (5), 1143–1170.

Ninno, F., Tsui, J., Balabani, S., Diaz-Zuccarini, V., 2023. A systematic review of clinical and biomechanical engineering perspectives on the prediction of restenosis in coronary and peripheral arteries. JVS-Vasc. Sci. 100128. http://dx.doi.org/10.1016/j.jvssci.2023.100128.

Nobuyoshi, M., Kimura, T., Nosaka, H., Mioka, S., Ueno, K., Yokoi, H., Hamasaki, N., Horiuchi, H., Ohishi, H., 1988. Restenosis after successful percutaneous transluminal coronary angioplasty: serial angiographic follow-up of 229 patients. J. Am. Coll. Cardiol. 12 (3), 616–623.

Nolan, D., Lally, C., 2018. Coupled finite element–agent-based models for the simulation of vascular growth and remodeling. In: Numerical Methods and Advanced Simulation in Biomechanics and Biological Processes. Elsevier, pp. 283–300.

Olsen, L., Sherratt, J.A., Maini, P.K., 1995. A mechanochemical model for adult dermal wound contraction and the permanence of the contracted tissue displacement profile. J. Theoret. Biol. 177 (2), 113–128.

Pasterkamp, G., de Kleijn, D.P., Borst, C., 2000. Arterial remodeling in atherosclerosis, restenosis and after alteration of blood flow: potential mechanisms and clinical implications. Cardiovasc. Res. 45 (4), 843–852. http://dx.doi.org/10.1016/S0008-6363(99)00377-6.

Popa-Fotea, N.-M., Ferdoschi, C.-E., Micheu, M.-M., 2023. Molecular and cellular mechanisms of inflammation in atherosclerosis. Front. Cardiovascul. Med. 10, 1200341. http://dx.doi.org/10.3389/fcvm.2023.1200341.

Pot, S.A., Liliensiek, S.J., Myrna, K.E., Bentley, E., Jester, J.V., Nealey, P.F., Murphy, C.J., 2010. Nanoscale topography–Induced modulation of fundamental cell behaviors of rabbit corneal keratocytes, fibroblasts, and myofibroblasts. Invest. Ophthalmol. Vis. Sci. 51 (3), 1373–1381. http://dx.doi.org/10.1167/iovs.09-4074.

Rodriguez-Granillo, G.A., Serruys, P.W., Garcia-Garcia, H.M., Aoki, J., Valgimigli, M., van Mieghem, C.A.G., McFadden, E., de Jaegere, P.P.T., de Feyter, P., 2006. Coronary artery remodelling is related to plaque composition. 2005/06/17 Heart (British Cardiac Society) 92 (3), 388–391. http://dx.doi.org/10.1136/hrt.2004.057810.

Schaan, B.D., Quadros, A.S., Sarmento-Leite, R., De Lucca, G., Bender, A., Bertoluci, M., 2007. 'Correction:' serum transforming growth factor beta-1 (TGF-beta-1) levels in diabetic patients are not associated with pre-existent coronary artery disease. Cardiovascul. Diabetol. 6 (1), 19.

Schwartz, S.M., Campbell, G.R., Campbell, J.H., 1986. Replication of smooth muscle cells in vascular disease. Circ. Res. 58 (4), 427–444.

Tracy, R.E., 1997. Declining density of intimal smooth muscle cells as a precondition for atheronecrosis in the coronary artery. Virchows Archiv 430 (2), 155–162.

Ueno, K., Morita, N., Kojima, Y., Takahashi, H., Esaki, M., Kondo, H., Ando, Y., Yamada, M., Kosokabe, T., 2023. Serial quantitative angiographic study of target lumen enlargement after drug-coated balloon angioplasty for native coronary artery disease. Catheter. Cardiovasc. Interv. 101 (4), 713–721. http://dx.doi.org/10.1002/ccd.30598.

Wilson, J.S., Baek, S., Humphrey, J.D., 2012. Importance of initial aortic properties on the evolving regional anisotropy, stiffness and wall thickness of human abdominal aortic aneurysms. J. R. Soc. Interface 9 (74), 2047–2058.